Journal of
Mechanics of
Materials and Structures

**THREE-DIMENSIONAL TREFFTZ COMPUTATIONAL GRAINS
FOR THE MICROMECHANICAL MODELING OF HETEROGENEOUS MEDIA
WITH COATED SPHERICAL INCLUSIONS**

Guannan Wang, Leiting Dong, Junbo Wang and Satya N. Atluri

∎
∎
msp

msp

THREE-DIMENSIONAL TREFFTZ COMPUTATIONAL GRAINS
FOR THE MICROMECHANICAL MODELING OF HETEROGENEOUS MEDIA
WITH COATED SPHERICAL INCLUSIONS

Guannan Wang, Leiting Dong, Junbo Wang and Satya N. Atluri

Three-dimensional computational grains based on the Trefftz method (TCGs) are developed to directly model the micromechanical behavior of heterogeneous materials with coated spherical inclusions. Each TCG is polyhedral in geometry and contains three phases: an inclusion, the surrounded coating (or interphase) and the matrix. By satisfying the 3D Navier's equations exactly, the internal displacement and stress fields within the TCGs are expressed in terms of the Papkovich–Neuber (P–N) solutions, in which spherical harmonics are employed to further express the P–N potentials. Further, the Wachspress coordinates are adopted to represent the polyhedral-surface displacements that are considered as nodal shape functions, in order to enforce the compatibility of deformations between two TCGs. Two techniques are developed to derive the local stiffness matrix of the TCGs: one is directly using the multi-field boundary variational principle (MFBVP) while the other is first applying the collocation technique for the continuity conditions within and among the grains and then employing a primal-field boundary variational principle (PFBVP). The local stress distributions at the interfaces between the 3 phases, as well as the effective homogenized material properties generated by the direct micromechanical simulations using the TCGs, are compared to other available analytical and numerical results in the literature, and good agreement is always obtained. The material and geometrical parameters of the coatings/interphases are varied to test their influence on the homogenized and localized responses of the heterogeneous media. Finally, the periodic boundary conditions are applied to the representative volume elements (RVEs) that contain one or more TCGs to model the heterogeneous materials directly.

1. Introduction

Heterogeneous materials reinforced with spherical-shaped inclusions have been widely applied in the aviation industry and the automobile industry due to their higher property-to-volume ratios relative to the monoclinic materials. In recent years, the effect of the interfaces between the inclusions and the matrices in particle-filled composites has received increasing attention because of the need to tailor the composite materials to meet specific requirements. Thus a good understanding of interfacial effects in composites, and establishing effective and highly efficient numerical models, when coatings/interfaces are considered, will be beneficial for the design and development of coated particulate composites.

Various classical micromechanical models were generalized to study the coated particulate composites. For example, the initial composite spherical assemblage (CSA) model proposed by Hashin [1962] was generalized to the three-phase domain to study the elastic moduli of coated particulate composites [Qiu

and Weng 1991; Herve and Zaoui 1993] or mineral materials [Nguyen et al. 2011]. The (generalized) self-consistent scheme (GSCS) was also employed to study the multiphase heterogeneous materials [Cherkaoui et al. 1994; Quang and He 2007]; The Mori–Tanaka (M–T) model was modified to calculate the properties of composites reinforced with uniformly distributed particles with interphases [Jiang et al. 2009]. The classical semi-analytical homogenization techniques largely provide the currently available tools, and even provide explicit expressions in the analysis of coated particulate composites, and thus have gained wide acceptance within the communities of mechanics and materials. However, most of these models are based on the assumption of the mean-field homogenization which only predicts accurate effective properties but cannot effectively recover the local inter-phase stress distributions, which are essentially important in the prediction of the possible failures and damages in the lifetime of heterogeneous materials.

Compared to the classical homogenization techniques, the simple finite-element (FE) methods can overcome the disadvantages mentioned above. The finite element method [Marur 2004; Liu et al. 2005; Tsui et al. 2006; Zhang et al. 2007; Jiang et al. 2008] has been widely used in investigating various aspects of particulate composites with coatings/interfaces, including computing the homogenized moduli, local stress concentrations, damage, and strengthening. However, the disadvantages of these simple finite elements are also well-known, such as unsatisfactory performance in problems which involve constraints (shear/membrane/incompressibility locking), low convergence rates for problems which are of singular nature (stress concentration problems and fracture mechanics problems), difficulty to satisfy higher-order continuity requirements (plates and shells), sensitivity to mesh distortion, etc. In order to capture the stress field accurately, the usual finite element methods involve extensive and laborious mesh generation, and very fine meshes involving large computational costs. Taking Figure 1, left, as an example [Chen et al. 2016; 2017], a total of 3952 hexahedron linear elements are adopted to discretize a single grain with an inclusion. If an RVE of a heterogeneous composite has to be modeled, with say a hundred or thousand grains, to not only generate effective properties but also capture the stress concentrations at the interfaces of inhomogeneities, the usual finite element method becomes almost impossible to be applied without using very high-performance super computers. Some other numerical techniques were also proposed to improve the stability and accuracy of the FE methods in micromechanical modeling of complex microstructures, for instance, fast Fourier transforms (FFT) [Moulinec and Suquet 1998; Michel et al. 2000], extended finite element method (XFEM) [Yvonnet et al. 2011; Zhu et al. 2011], etc.

In order to effectively reduce the computational efforts without sacrificing the accuracy, the concept of Trefftz computational grains (TCGs) was developed by Dong and Atluri [2012c; 2012b; 2012a], and Bishay and Atluri [2013; 2014; 2015; Bishay et al. 2014] used radial basis functions as well as Trefftz formulation based computational grains for multi-functional composites. Instead of applying the simple finite element discretization of the microstructures, an arbitrarily shaped TCG composed of fiber/coating/matrix constituents is treated as a "super" element (Figure 1, right), whose internal displacement and traction fields are represented by the Trefftz solutions. Based on the Trefftz concept [Qin 2005] of using the complete analytical solutions which satisfy the Navier's equations of elasticity, the development of the highly accurate and efficient two- and three-dimensional polyhedral computational grains was achieved. It should be noted that the idea of the VCFEM was initially proposed to investigate the particle reinforced composites [Ghosh et al. 1995; Moorthy and Ghosh 1998] in the 2D cases. However, the VCFEM developed in [Ghosh et al. 1995; Moorthy and Ghosh 1998] was based on the hybrid-stress finite element method, with both domain and boundary integrations for each Voronoi
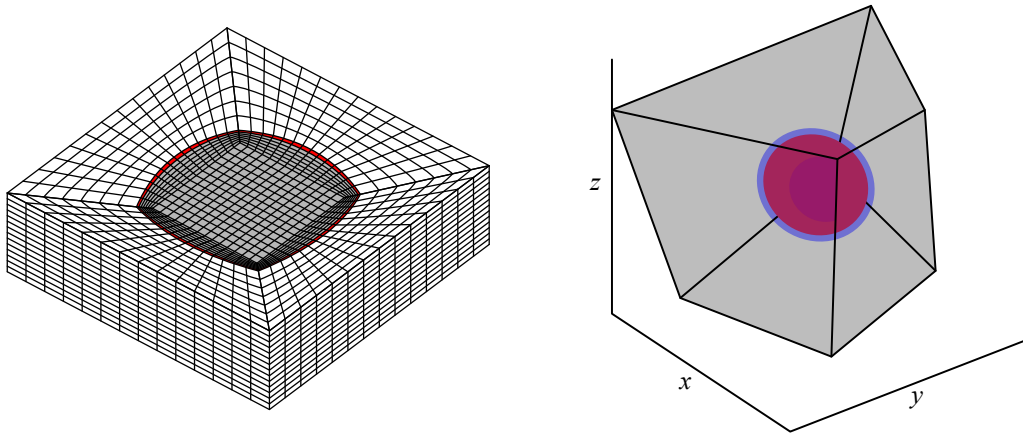
Figure 1. Left: the usual FE mesh discretization of spherical particulate composites [Chen et al. 2016; 2017]. Right: a single polyhedral Trefftz computational grain (TCG) with three phases.

element, and adopted incomplete stress functions (in the hybrid stress finite element method), leading to the inefficient computational efforts and highly inaccurate internal and interfacial stress distributions. The new version of the TCGs [Dong and Atluri 2012a; 2012b; 2012c] differ from the hybrid stress VCFEM in [Ghosh et al. 1995; Moorthy and Ghosh 1998] in the following ways 1) a complete Trefftz trial displacement solution is assumed in the TCG by satisfying both the equilibrium and compatibility conditions a priori; 2) only boundary integrals are involved in the newly developed TCG, ensuring its better accuracy and efficiency in the micromechanical computations. All of these characteristics prove that the Trefftz computational grains are reliable tools in generating both effective properties as well as the inter-phase local stress field distributions in the micromechanics of heterogeneous materials.

Based on the framework established by Dong and Atluri [2012a; 2012b; 2012c], the Trefftz computational grains (TCGs) are generalized in this paper, for the micromechanical modeling of heterogeneous materials reinforced with coated particles (or particles with interphases). By avoiding the large-scale mesh discretization of a microstructure within the normal FE framework, each arbitrarily shaped TCG in the present situation is composed of a particulate inclusion, a coating/interphase and the surrounding matrix phase, Figure 1, right. The trial displacement solutions of each constituent are obtained by employing Papkovich–Neuber (P–N) solutions [Lurie 2005], in which the P–N potentials are further represented by the spherical harmonics. Two approaches are then used to develop the local stiffness matrix of the TCGs: First, a multi-field boundary variational principle is proposed to enforce continuities between adjacent constituents and TCGs, as well as the external boundary conditions, if any; Second, the collocation technique [Dong and Atluri 2012b; 2012c; Wang et al. 2018] is applied to satisfy the interfacial continuity conditions, while a primal-field boundary variational principle is employed to satisfy the interphase continuities and the boundary conditions, a technique which we name as CPFBVP. Both approaches generate accurate predictions as compared to the currently available semi-analytical and numerical results. Finally, an easy implementation of periodic boundary conditions (PBCs) is achieved on the representative volume elements by surface-to-surface constraint scheme.

The remainder of the paper is organized as follows: Section 2 solves the displacement fields in each constituent of a TCG in terms of the P–N solutions and develops the local stiffness matrix of the TCGs. Section 3 validates the homogenized moduli and local inter-phase stress distributions through comparing with the CSA and detailed fine-mesh FE results. The influence of the coatings/interphases on the various properties of composites materials is thoroughly investigated in Section 4. Finally, the effects of the periodic boundary conditions on the RVEs are studied in Section 5. Section 6 concludes this contribution.

2. Development of polyhedral Trefftz computational grains (TCGs) with coated spherical inclusions/voids

2.1. *Boundary displacement field for a polyhedral TCG.* For an arbitrarily polyhedral-shaped TCG in the 3D space, each surface is a polygon, Figure 1, right. Constructing an inter-TCG compatible displacement on the boundary of the polyhedral element is not as simple as that for the 2D version. One way of doing this is to use barycentric coordinates as nodal shape functions on each polygonal face of the 3D TCGs.

Consider a polygonal face V_n with n nodes $x^1, x^2, \ldots, x^n$, within barycentric coordinates, denoted as λ_i ($i = 1, 2, \ldots, n$). The coordinates λ_i depend only on the position vector x^i. To obtain a good performance of a TCG, we only consider barycentric coordinates that satisfy the following properties:

1. Being nonnegative: $\lambda_i \leq 0$ in the polygon V_n.

2. Smoothness: λ_i is at least C^1 continuous in the polygon V_n.

3. Linearity along each edge that composes the polygon V_n.

4. Linear completeness: For any linear function $f(x)$, the equation $f(x) = \sum_{i=1}^{n} f(x^i)\lambda_i$ holds.

5. Partition of unity: $\sum_{i=1}^{n} \lambda_i \equiv 1$.

6. Dirac delta property: $\lambda_i(x^j) = \delta_{ij}$.

Among the many barycentric coordinates that satisfy these conditions, Wachspress coordinate is the most simple and efficient [Wachspress 1975].

A point $x \in V_n$ within the polygon is determined in terms of two parameters: B_i as the area of the triangle with the vertices of x^{i-1}, x^i and x^{i+1}, and $A_i(x)$ as the area of the triangle with vertices of x, x^i and x^{i+1}, Figure 2. Thus, the Wachspress coordinate of the point x can be written as

$$\lambda_i(x) = \frac{w_i(x)}{\sum_{j=1}^{n} w_j(x)}, \tag{1}$$

wherein the weight function is defined as

$$w_i(x) = \frac{B_i(x^{i-1}, x^i, x^{i+1})}{A_{i-1}(x^{i-1}, x^i, x)A_i(x^i, x^{i+1}, x)}. \tag{2}$$

The inter-TCG compatible displacement field is therefore expressed in terms of the nodal shape functions for the polygonal surface vertices and the nodal displacements in the Cartesian coordinates:

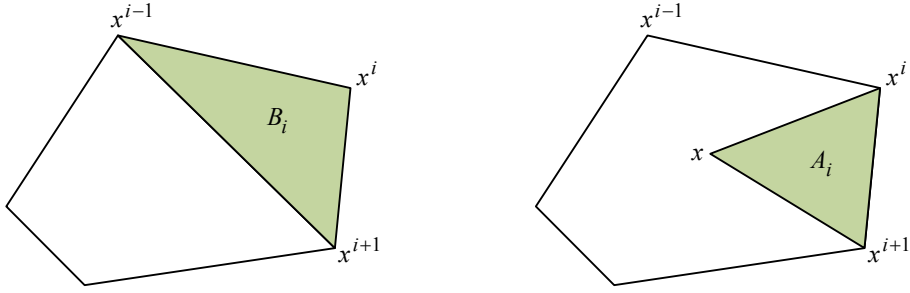$$\tilde{u}_i(x) = \sum_{k=1}^{n} \lambda_k(x) u_i(x^k) \quad x \in V_n, V_n \subset \partial\Omega^e, \tag{3}$$

Figure 2. Definition of Wachspress coordinates on each surface of a polyhedron.

where $\partial\Omega^e$ denotes the surface of each TCG.

2.2. *The governing equations of linear elasticity for each phase of the TCGs.* As shown in Figure 3, the solutions of the 3D linear elasticity for the matrix and inclusion phases should satisfy the equilibrium equations, strain-displacement compatibilities, as well as the constitutive relations in each element Ω^e:

$$\sigma_{ij,j}^k + f_i^k = 0, \tag{4}$$
$$\varepsilon_{ij}^k = \tfrac{1}{2}\big(u_{i,j}^k + u_{j,i}^k\big), \tag{5}$$
$$\sigma_{ij}^k = \lambda^k \varepsilon_{mm}^k \delta_{ij} + 2\mu^k \varepsilon_{ij}^k, \tag{6}$$

where the superscript $k = m, c, p$ denotes the matrix, the coating and the inclusion (particle) phases, u_i^k, ε_{ij}^k, σ_{ij}^k are the displacement, strain and stress components, f_i^k is the body force, which is neglected in this situation, and Here, λ^k and μ^k are the Lamé constants of each phase.

At the interfaces between the constituents within each TCG, the displacement continuities and traction reciprocities can be written as

$$u_i^m = u_i^c \quad \text{at } \partial\Omega_c^e, \tag{7}$$
$$-n_j\sigma_{ij}^m + n_j\sigma_{ij}^c = 0 \quad \text{at } \partial\Omega_c^e, \tag{8}$$
$$u_i^c = u_i^p \quad \text{at } \partial\Omega_p^e, \tag{9}$$
$$-n_j\sigma_{ij}^c + n_j\sigma_{ij}^p = 0 \quad \text{at } \partial\Omega_p^e, \tag{10}$$

where $\partial\Omega_c^e$ and $\partial\Omega_p^e$ are the outer surfaces of the coating and inclusion phases, respectively. The external boundary conditions for each TCG can be written as

$$u_i^m = \bar{u}_i \quad \text{at } S_u^e, \tag{11}$$
$$n_j\sigma_{ij}^m = \bar{t}_i \quad \text{at } S_t^e, \tag{12}$$
$$(n_j\sigma_{ij}^m)^+ + (n_j\sigma_{ij}^m)^- = 0 \quad \text{at } \rho^e, \tag{13}$$

where S_u^e, S_t^e and ρ^e are displacement, traction and other boundaries of the domain Ω^e, respectively, and $\partial\Omega^e = S_u^e \cup S_t^e \cup \rho^e$. $\bar{u}_i$, $\bar{t}_i$ are the prescribed boundary displacement and traction components when they exist.
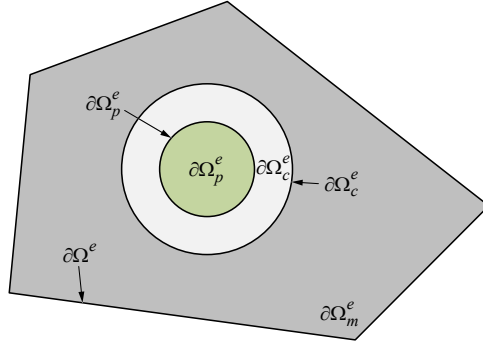
Figure 3. A polyhedral Trefftz computational grain and its nomenclature.

2.3. *Papkovich–Neuber solutions as the trial internal displacement fields within each TCG.* Navier's equation can be derived from (4)–(6):

$$(\lambda^k + \mu^k)\, u^k_{j,ji} + \mu^k \Delta u^k_i = 0. \tag{14}$$

Solving the displacement components directly from (14) is a rather difficult task. Papkovich [1932] and Neuber [1934] suggested that the solutions can be represented in the forms of harmonic functions:

$$\boldsymbol{u}^k = \frac{4(1 - \nu^k)\boldsymbol{B}^k - \nabla(\boldsymbol{R} \cdot \boldsymbol{B}^k + B^k_0)}{2\mu^k}, \tag{15}$$

where B^k_0 and $\boldsymbol{B}_k = \begin{bmatrix} B^k_1 & B^k_2 & B^k_3 \end{bmatrix}^T$ are scalar and vector harmonic functions. $\boldsymbol{R}$ is the position vector. μ^k is the shear modulus of the k-th constituent.

The number of independent harmonic functions in (15) is more than the number of independent displacement components. Therefore, it is desired to keep only three of the four harmonic functions. Thus, by dropping B^k_0 we have the following solution:

$$\boldsymbol{u}^k = \frac{4(1 - \nu^k)\boldsymbol{B}^k - \nabla \boldsymbol{R} \cdot \boldsymbol{B}^k}{2\mu^k}. \tag{16}$$

The general solution of (16) is complete for an infinite domain external to a closed surface. However, for a simply-connected domain, equation (16) is only complete when $\nu \neq 0.25$. M. G. Slobodyansky proved that, by expressing B^k_0 as a specific function of $\boldsymbol{B}^k$, the derived general solution of (14) is complete for a simply-connected domain with any valid Possion's ratio:

$$\boldsymbol{u}^k = \frac{4(1 - \nu^k)\boldsymbol{B}^k + \boldsymbol{R} \cdot \nabla \boldsymbol{B}^k - \boldsymbol{R}\nabla \cdot \boldsymbol{B}^k}{2\mu^k}. \tag{17}$$

The harmonic vector $\boldsymbol{B}$ needs to be further expressed using the special functions to define various domain surfaces. To accommodate the spherical inclusion and its coating, spherical harmonics are adopted and introduced in the next section.

2.4. *Spherical harmonics.* Consider a point with Cartesian coordinates x_1, x_2, x_3 and the corresponding spherical coordinates $q^1 = R$, $q^2 = \theta$, $q^3 = \varphi$ having the following relationship:

$$x_1 = R \sin\theta \cos\varphi, \quad x_2 = R \sin\theta \sin\varphi, \quad x_3 = R \cos\theta. \tag{18}$$

From (18), we have

$$\frac{\partial x_1}{\partial R} = \sin\theta \cos\varphi, \quad \frac{\partial x_1}{\partial \theta} = R \cos\theta \cos\varphi, \quad \frac{\partial x_1}{\partial \varphi} = -R \sin\theta \sin\varphi,$$

$$\frac{\partial x_2}{\partial R} = \sin\theta \sin\varphi, \quad \frac{\partial x_2}{\partial \theta} = R \cos\theta \sin\varphi, \quad \frac{\partial x_2}{\partial \varphi} = R \sin\theta \cos\varphi, \tag{19}$$

$$\frac{\partial x_3}{\partial R} = \cos\theta, \quad \frac{\partial x_3}{\partial \theta} = -R \sin\theta, \quad \frac{\partial x_3}{\partial \varphi} = 0,$$

and

$$\frac{\partial q^s}{\partial x_k} = \frac{1}{H_s^2} \frac{\partial x_k}{\partial q^s}, \quad \frac{\partial \mathbf{R}}{\partial q^r} \cdot \frac{\partial \mathbf{R}}{\partial q^s} = \delta_{rs} H_r H_s, \tag{20}$$

where

$$H_1 = H_R = 1, \quad H_2 = H_\theta = R, \quad H_3 = H_\varphi = R \sin\theta, \tag{21}$$

are called Lamé's coefficients. By defining a set of orthonormal base vectors of the spherical coordinate system:

$$\mathbf{g}_r = \frac{1}{H_r} \frac{\partial \mathbf{R}}{\partial q^r}, \tag{22}$$

we have

$$\frac{\partial \mathbf{g}_R}{\partial R} = 0, \quad \frac{\partial \mathbf{g}_R}{\partial \theta} = \mathbf{g}_\theta, \quad \frac{\partial \mathbf{g}_R}{\partial \varphi} = \mathbf{g}_\varphi \sin\theta,$$

$$\frac{\partial \mathbf{g}_\theta}{\partial R} = 0, \quad \frac{\partial \mathbf{g}_\theta}{\partial \theta} = -\mathbf{g}_R, \quad \frac{\partial \mathbf{g}_\theta}{\partial \varphi} = \mathbf{g}_\varphi \cos\theta, \tag{23}$$

$$\frac{\partial \mathbf{g}_\varphi}{\partial R} = 0, \quad \frac{\partial \mathbf{g}_\varphi}{\partial \theta} = 0, \quad \frac{\partial \mathbf{g}_\varphi}{\partial \varphi} = -(\mathbf{g}_R \sin\theta + \mathbf{g}_\theta \sin\theta).$$

Therefore, the Laplace operator of a scalar f has the following form:

$$\nabla^2 f = \nabla \cdot \nabla f = \frac{1}{H_r} \mathbf{g}_r \frac{\partial}{\partial q_r} \cdot \frac{1}{H_s} \mathbf{g}_s \frac{\partial f}{\partial q_s}$$

$$= \frac{1}{R} \left[\frac{\partial}{\partial R} R^2 \frac{\partial f}{\partial R} + \frac{\partial}{\partial \xi} (1 - \xi^2) \frac{\partial f}{\partial \xi} + \frac{1}{1 - \xi^2} \frac{\partial f}{\partial \lambda^2} \right], \tag{24}$$

where the new variable $\xi = \cos\theta$ is introduced. By assuming that $f = L(R) M(\xi) N(\varphi)$ and using k^2 and $n(n+1)$ as separating constants, it can be shown that L, M, N satisfy the following equations:

$$N''(\varphi) + k^2 N(\varphi) = 0, \tag{25}$$

$$[(1 - \xi^2) M'(\xi)]' + \left[n(n+1) - \frac{k^2}{1 - \xi^2} \right] M(\xi) = 0, \tag{26}$$

$$[R^2 L'(R)]' - n(n+1) L(R) = 0. \tag{27}$$

Equation (25) leads to particular solutions $\cos k\varphi$ and $\sin k\varphi$ for a nonnegative integer k, because of the periodicity of $N(\varphi)$. Equation (26), which is clearly the associated Legendre's differential equation, leads to the associated Legendre's functions of the first and the second kinds, where only the associated Legendre's functions of the first kind are valid for constructing $M(\xi)$. Denoting them as $P_n^k(\xi)$, we have

$$P_n^k(\xi) = (-1)^k (1 - \xi^2)^{k/2} \frac{d^k}{d\xi^k} P_n(\xi), \quad P_n(\xi) = \frac{1}{2^2 n!} \left[\frac{d^n}{d\xi^n} (\xi^2 - 1)^n \right]. \tag{28}$$

The product of $M(\xi)N(\varphi)$ are called spherical surface harmonics, and can be normalized to be

$$\begin{aligned} Y_n^k(\theta, \varphi) &= \sqrt{\frac{2n+1}{4\pi} \frac{(n-k)!}{(n+k)!}} \, P_n^k(\cos(\theta)) \, e^{ik\varphi} \\ &= \sqrt{\frac{2n+1}{4\pi} \frac{(n-k)!}{(n+k)!}} \, P_n^k(\cos(\theta)) [\cos(k\varphi) + i \sin(k\varphi)] \\ &= YC_n^k(\theta, \varphi) + i \, YS_n^k(\theta, \varphi), \end{aligned} \tag{29}$$

such that

$$\int_0^{2\pi} \int_0^\pi Y_n^k(\theta, \varphi) \bar{Y}_{n'}^{k'}(\theta, \varphi) \sin\theta \, d\theta \, d\varphi = \delta_{kk'} \, \delta_{nn'}. \tag{30}$$

Finally, equation (27) leads to particular solutions R^n and $R^{-(m+1)}$. For different problems, different forms of $L(R)$ should be used, which leads to different forms of spherical harmonics. For the internal problem of a sphere, only R^n is valid. f can be expanded as

$$f_p = \sum_{n=0}^{\infty} R^n \left\{ a_0^0 YC_0^0(\theta, \varphi) + \sum_{j=1}^{n} \left[a_n^j YC_n^j(\theta, \varphi) + b_n^j YS_n^j(\theta, \varphi) \right] \right\}. \tag{31}$$

For external problems in an infinite domain, only $R^{-(m+1)}$ is valid, f can be expanded as

$$f_k = \sum_{m=0}^{\infty} R^{-(m+1)} \left\{ c_0^0 YC_0^0(\theta, \varphi) + \sum_{j=1}^{m} \left[c_m^j YC_m^j(\theta, \varphi) + d_m^j YS_m^j(\theta, \varphi) \right] \right\}, \tag{32}$$

where a_n^j, b_n^j, c_m^j and d_m^j are the unknown coefficients that can be solved through their implementations into the elasticity solutions and variational principles. The numbers of the unknown coefficients depend on the harmonic terms employed in the calculations, which are further dependent on the complexity of the problems.

As is mentioned in [Liu 2007a; 2007b], the above trial functions will lead to ill-conditioned systems of equations when being applied in the Trefftz method to numerically solve a boundary value problem. Thus, the characteristic lengths are introduced to scale the equations (31) and (32) [Dong and Atluri 2012b; 2012c; Liu 2007a; 2007b] to better condition the relevant matrices that arise in the Trefftz method.

For a specific domain of interest, two characteristic lengths R_{non} and R_{sig} are defined, which are respectively the maximum and minimum values of the radial distance R of points where boundary conditions are specified. Therefore, $(R/R_{\text{non}})^n$ and $(R_{\text{sig}}/R)^{-(m+1)}$ is confined between 0 and 1 for any positive

integers n and m. Harmonics are therefore scaled as

$$f_p = \sum_{n=0}^{\infty} \left(\frac{R}{R_{\text{non}}}\right)^n \left\{ a_0^0 Y C_0^0(\theta, \varphi) + \sum_{j=1}^{n} [a_n^j Y C_n^j(\theta, \varphi) + b_n^j Y S_n^j(\theta, \varphi)] \right\}, \tag{33}$$

$$f_k = \sum_{m=0}^{\infty} \left(\frac{R}{R_{\text{sig}}}\right)^{-(m+1)} \left\{ c_0^0 Y C_0^0(\theta, \varphi) + \sum_{j=1}^{m} [c_m^j Y C_m^j(\theta, \varphi) + d_m^j Y S_m^j(\theta, \varphi)] \right\}. \tag{34}$$

2.5. *Trefftz trial displacement fields.* For an element with an inclusion as well as the coating of spherical geometries, the displacement field in the inclusion can be derived by substituting the nonsingular harmonics, equation (33) into (17):

$$\boldsymbol{u}^p = [4(1 - \nu^p)\boldsymbol{B}^{pi} + \boldsymbol{R} \cdot \nabla \boldsymbol{B}^{pi} - \boldsymbol{R}\nabla \cdot \boldsymbol{B}^{pi}]/(2\mu^p). \tag{35}$$

The displacement fields in the matrix and the coating phases are the summation of $\boldsymbol{u}^{ki}$ (the nonsingular part) and $\boldsymbol{u}^{ke}$ (the singular part, with the singularity being located at the center of the inclusion). $\boldsymbol{u}^{ki}$ can be derived by substituting (33) into (17), and $\boldsymbol{u}^{ke}$ can be derived by substituting (34) into (16):

$$\begin{aligned}
\boldsymbol{u}^k &= \boldsymbol{u}^{ki} + \boldsymbol{u}^{ke} \quad (k = m, c), \\
\boldsymbol{u}^{ki} &= [4(1 - \nu^k)\boldsymbol{B}^{ki} + \boldsymbol{R} \cdot \nabla \boldsymbol{B}^{ki} - \boldsymbol{R}\nabla \cdot \boldsymbol{B}^{ki}]/(2\mu^k), \\
\boldsymbol{u}^{ke} &= [4(1 - \nu^k)\boldsymbol{B}^{ke} - \nabla \boldsymbol{R} \cdot \boldsymbol{B}^{ke}]/(2\mu^k).
\end{aligned} \tag{36}$$

A more detailed illustration is given in [Dong and Atluri 2012b]. The expressions of strains and stresses can be then calculated by using *Wolfram Mathematica 8.0*, and are too complicated to be explicitly presented here. To obtain the converged results in this presentation, we let $n = 3$ for the nonsingular solution of the particulate phase, equation (35), and $n = 4$, $m = 3$ for the elastic solutions of the coating and matrix phases, equation (36).

2.6. *TCGs through the multi-field boundary variational principle.* The four-field energy functional of the 3-phase Trefftz computational grains can be expressed for an elastic coated particulate reinforced heterogeneous media:

$$\pi(\tilde{u}_i^m, u_i^m, u_i^c, u_i^p) = \sum_e \left\{ \int_{\partial\Omega^e + \partial\Omega_c^e} -\frac{1}{2}t_i^m u_i^m \, dS + \int_{\partial\Omega^e} t_i^m \tilde{u}_i^m \, dS + \int_{\partial\Omega_c^e} t_i^m u_i^c \, dS \right\}$$
$$+ \sum_e \int_{\partial\Omega_c^e + \partial\Omega_p^e} \frac{1}{2}t_i^c u_i^c \, dS + \sum_e \left\{ \int_{\partial\Omega_p^e} -\frac{1}{2}t_i^p u_i^p \, dS + \int_{\partial\Omega_p^e} t_i^p u_i^c \, dS \right\} - \int_{S_t} \bar{t}_i \tilde{u}_i \, dS, \tag{37}$$

where the matrix strain energy, coating strain energy, inclusion strain energy, as well as the work done by external force are included. A first variation of the functional in (37) yields the Euler–Lagrange equations expressed in (7)–(13).

By assuming the displacement and stress fields in the vector forms:

$$\tilde{u}_m = \tilde{N}q \qquad \text{at } \partial\Omega^e \tag{38}$$

$$u_m = N_m\alpha \qquad \text{in } \Omega_m^e \tag{39a}$$

$$t_m = R_m\alpha \qquad \text{at } \partial\Omega^e, \partial\Omega_c^e \tag{39b}$$

$$u_c = N_c\beta \qquad \text{in } \Omega_c^e \tag{40a}$$

$$t_c = R_c\beta \qquad \text{at } \partial\Omega_c^e, \partial\Omega_p^e \tag{40b}$$

$$u_p = N_p\gamma \qquad \text{in } \Omega_p^e \tag{41a}$$

$$t_p = R_p\gamma \qquad \text{at } \partial\Omega_p^e \tag{41b}$$

and substituting them into (37), the finite element equations can be deduced by making the first variation:

$$\delta\begin{Bmatrix} q \\ \beta \end{Bmatrix}^T \begin{bmatrix} G_{\alpha q}^T H_{\alpha\alpha}^{-1} G_{\alpha q} & G_{\alpha q}^T H_{\alpha\alpha}^{-1} G_{\alpha\beta} \\ G_{\alpha\beta}^T H_{\alpha\alpha}^{-1} G_{\alpha q} & G_{\alpha\beta}^T H_{\alpha\alpha}^{-1} G_{\alpha\beta} + H_{\beta\beta} + G_{\beta\gamma}^T H_{\gamma\gamma}^{-1} G_{\beta\gamma} \end{bmatrix} \begin{Bmatrix} q \\ \beta \end{Bmatrix} = \delta\begin{Bmatrix} q \\ \beta \end{Bmatrix}^T \begin{Bmatrix} Q \\ 0 \end{Bmatrix}, \tag{42}$$

where α and γ are eliminated in the above equation and expressed in terms of β and q, and

$$H_{\alpha\alpha} = \int_{\partial\Omega^e + \partial\Omega_c^e} R_m^T N_m \, dS, \quad H_{\beta\beta} = \int_{\partial\Omega_c^e + \partial\Omega_p^e} R_c^T N_c \, dS, \quad H_{\gamma\gamma} = \int_{\partial\Omega_p^e} R_p^T N_p \, dS,$$

$$G_{\alpha\beta} = \int_{\partial\Omega_c^e} R_m^T N_c \, dS, \quad G_{\alpha q} = \int_{\partial\Omega^e} R_m^T \tilde{N} \, dS, \quad G_{\beta\gamma} = \int_{\partial\Omega_p^e} R_c^T N_p \, dS, \quad Q = \int_{\partial\Omega^e} \tilde{N}^T \bar{t} \, dS.$$

By defining $k_{qq} = G_{\alpha q}^T H_{\alpha\alpha}^{-1} G_{\alpha q}$, $k_{q\beta} = G_{\alpha q}^T H_{\alpha\alpha}^{-1} G_{\alpha\beta}$ and $k_{\beta\beta} = G_{\alpha\beta}^T H_{\alpha\alpha}^{-1} G_{\alpha\beta} + H_{\beta\beta} + G_{\beta\gamma}^T H_{\gamma\gamma}^{-1} G_{\beta\gamma}$, the local stiffness matrix of a TCG is

$$k_{\text{local}} = k_{qq} - k_{q\beta} \, k_{\beta\beta} \, k_{q\beta}^T, \tag{43}$$

with the vectors of unknown coefficients in terms of the nodal displacement field:

$$\alpha = H_{\alpha\alpha}^{-1}\big(G_{\alpha q} - G_{\alpha\beta}k_{\beta\beta}^{-1}k_{q\beta}^T\big)q,$$
$$\beta = -k_{\beta\beta}^{-1}k_{q\beta}^T q, \tag{44}$$
$$\gamma = -H_{\gamma\gamma}^{-1}G_{\beta q}k_{\beta\beta}^{-1}k_{q\beta}^T q.$$

It should be noted that the six rigid-body modes in the field expressions should be eliminated for the application of MFBVP but not for the CPFBVP. By displaying the displacement and stress expressions in matrix forms, the following three modes only make contributions to the total resultant forces at the source point and should be taken out:

$$c_0^0 = \{1 \quad 0 \quad 0\}^T, \quad c_0^0 = \{0 \quad 1 \quad 0\}^T, \quad c_0^0 = \{0 \quad 0 \quad 1\}^T, \tag{45}$$

while the following modes need to be eliminated because they only contribute to the total resultant moments at the source point:

$$c_1^0 = \{1 \quad 0 \quad 0\}^T, \quad c_1^1 = \{0 \quad 0 \quad \sqrt{2}\}^T,$$
$$c_1^0 = \{0 \quad 1 \quad 0\}^T, \quad c_1^1 = \{0 \quad \sqrt{2} \quad 0\}^T,$$
$$c_1^0 = \{0 \quad 1 \quad 0\}^T, \quad d_1^1 = \{-1 \quad 0 \quad 0\}^T. \tag{46}$$

2.7. *TCGs through collocation and the primal-field boundary variational principle.* An alternative to the MFBVP is employing a collocation technique for the internal displacement continuity and traction reciprocity conditions between adjacent constituents and applying the primal field boundary variational principle for the inter-element conditions.

By using collocation technique, a certain number of collocation points are usually uniformly distributed along the interfaces of heterogeneities $\partial \Omega_c^e$, $\partial \Omega_p^e$ as well as the boundary of the elements $\partial \Omega^e$. The coordinates of the collocation points are denoted as follows: $x_i^{mh} \in \partial \Omega^e$, $h = 1, 2, \ldots$; $x_i^{ck} \in \partial \Omega_c^e$, $k = 1, 2, \ldots$; and $x_i^{pl} \in \partial \Omega_p^e$, $l = 1, 2, \ldots$.

For a TCG with a coated elastic inclusion, the conditions of displacement continuities and traction reciprocities are applied at the local collocation points of the interfaces between adjacent constituents:

$$u_i^m(x_j^{ck}, \boldsymbol{\alpha}) = u_i^c(x_j^{ck}, \boldsymbol{\beta}), \qquad x_j^{ck} \in \partial \Omega_c^e,$$
$$wt_i^m(x_j^{ck}, \boldsymbol{\alpha}) + wt_i^c(x_j^{ck}, \boldsymbol{\beta}) = 0, \quad x_j^{ck} \in \partial \Omega_c^e, \tag{47}$$

$$u_i^c(x_j^{pl}, \boldsymbol{\beta}) = u_i^p(x_j^{pl}, \boldsymbol{\gamma}), \qquad x_j^{pl} \in \partial \Omega_p^e,$$
$$wt_i^c(x_j^{pl}, \boldsymbol{\beta}) + wt_i^p(x_j^{pl}, \boldsymbol{\gamma}) = 0, \quad x_j^{pl} \in \partial \Omega_p^e, \tag{48}$$

as well as the relationship between internal displacements and nodal functions:

$$u_i^m(x_j^{mh}, \boldsymbol{\alpha}) = \tilde{u}_i(x_i^{mh}, \boldsymbol{q}) \quad x_j^{mh} \in \partial \Omega^e, \tag{49}$$

where the parameter "w" is used to balance the displacement and traction equations, avoiding the effect of the material properties on the discrepancy of the magnitude. In this situation $w = 1/(2\mu_c)$.

From the above relations, a system of equations can be easily set up for the unknown coefficients of different phases:

$$\boldsymbol{A}_{\alpha q}^e \boldsymbol{\alpha} = \boldsymbol{B}_{\alpha q}^e \boldsymbol{q}, \quad \boldsymbol{A}_{\alpha\beta}^e \boldsymbol{\alpha} = \boldsymbol{B}_{\alpha\beta}^e \boldsymbol{\beta}, \quad \boldsymbol{A}_{\beta\gamma}^e \boldsymbol{\beta} = \boldsymbol{B}_{\beta\gamma}^e \boldsymbol{\gamma}, \tag{50}$$

which yield to a system of equations as following:

$$\begin{bmatrix} \boldsymbol{A}_{\alpha\beta}^e & -\boldsymbol{B}_{\alpha\beta}^e & \boldsymbol{0} \\ \boldsymbol{0} & \boldsymbol{A}_{\beta\gamma}^e & -\boldsymbol{B}_{\beta\gamma}^e \\ \boldsymbol{A}_{\alpha q}^e & \boldsymbol{0} & \boldsymbol{0} \end{bmatrix} \begin{Bmatrix} \boldsymbol{\alpha} \\ \boldsymbol{\beta} \\ \boldsymbol{\gamma} \end{Bmatrix} = \begin{bmatrix} \boldsymbol{0} \\ \boldsymbol{0} \\ \boldsymbol{B}_{\alpha q}^{eT} \end{bmatrix}^T \boldsymbol{q}. \tag{51}$$

	E (GPa)	ν
Al_2O_3 Particle	390.0	0.24
SiC Coating	413.6	0.17
Al Matrix	74	0.33

Table 1. The material properties of a TCG composed of Al_2O_3/SiC/Al.

After relating the trial internal displacement expressions with nodal shape function of each TCG, a primal-field boundary variational principle is then introduced to derive the local stiffness matrix:

$$\pi_4(u_i) = \sum_e \left\{ \int_{\partial \Omega^e} \frac{1}{2} t_i u_i \, dS - \int_{S_t^e} \bar{t}_i u_i \, dS \right\}. \tag{52}$$

Substituting the displacement expressions into the above functional and making the first variation lead to

$$\sum_e \left(\delta q^T C_{\alpha q}^T M_{\alpha \alpha}^{-1} C_{\alpha q} q - \delta q^T Q \right) = 0, \tag{53}$$

in which $M_{\alpha \alpha} = \int_{\partial \Omega^e} R_m^T N_m \, dS$.

Remarks: Using MFBVP is plagued by LBB conditions because of the Lagrange multipliers involved [Babuška 1973; Brezzi 1974; Punch and Atluri 1984; Rubinstein et al. 1983], while CPFBVP avoids the LBB violation by introducing the collocation technique. In addition, only one matrix $M_{\alpha \alpha}$ is integrated in the CPFBVP, while several matrices are evaluated in the MFBVP. Thus, the CPFBVP should be more computationally efficient than the MFBVP, which is also proved by the following numerical examples.

3. Numerical validations

3.1. *Condition numbers.* As is introduced in the previous section, the characteristic parameters R_{non} and R_{sig} are introduced to scale the T-Trefftz trial functions. The magnitudes of R_{non} and R_{sig} are determined by the geometries of the investigated domains. Here we study the effect of the characteristic parameters on the condition numbers of the coefficient matrices involved in the calculations. In this example, a TCG with the material properties listed in Table 1 is investigated; see Figure 4. The dimensions of the TCG are $L \times W \times H = 200 \times 200 \times 200 \, \mu m^3$, and the outer radii of inclusion and coating are $R_p = 72.56 \, \mu m$ and $R_c = 79.82 \, \mu m$, respectively. Tables 2 and 3 list the condition numbers of the inverted matrices in both MFBVP and CPFBVP, with or without introducing R_{non} and R_{sig}. It can be easily observed that when the characteristic parameters are not adopted ($R_{non} = 1$ and $R_{sig} = 1$), the condition numbers are too large to generate accurate results. The usage of R_{non} and R_{sig} can significantly reduce the condition numbers and guarantee calculation precision.

3.2. *Patch test.* The one-element patch test is conducted in this section. The same element is considered with same geometrical parameters and material properties listed in Table 1; see Figure 4. A uniform loading is applied to the right face ($y = 100 \, \mu m$), while the essential boundary conditions are applied at the left face ($y = -100 \, \mu m$). The exact solutions for the deformation of a homogeneous cube can be

Matrix	Without R_{non}, R_{sig}	With R_{non}, R_{sig}
$H_{\alpha\alpha}$	3.819×10^{31}	1.678×10^{2}
$H_{\gamma\gamma}$	2.094×10^{10}	0.991×10^{2}

Table 2. Condition numbers of the matrices of (42) used in MFBVP.

Matrix	Without R_{non}, R_{sig}	With R_{non}, R_{sig}
$M_{\alpha\alpha}$	4.593×10^{33}	7.605×10^{4}

Table 3. Condition numbers of the matrix of (53) used in CPFBVP.
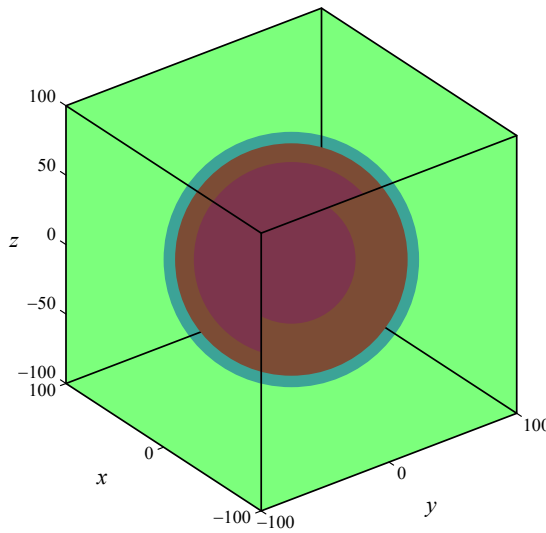
Figure 4. A TCG used to generate the condition numbers and patch test.

expressed as:

$$u_1 = -\frac{p\nu}{E}x_1, \quad u_2 = \frac{p}{E}x_2, \quad u_3 = -\frac{p\nu}{E}x_3, \tag{54}$$

which are compared with the numerical nodal displacement q on the right face, and the error is defined as

$$\Delta = \frac{\|q - q^{\text{exact}}\|}{\|q^{\text{exact}}\|}. \tag{55}$$

The errors generated by MFBVP and CPFBVP are 1.737×10^{-6} and 1.827×10^{-4}, respectively, indicating both approaches obtain results with high accuracy. The execution time of the MFBVP and CPFBVP to generate the local stiffness matrix of the TCG is 29.351 s and 6.51 s, respectively. The execution time of the MFBVP is a bit longer because the MFBVP involves more matrices to be integrated.

3.3. *Homogenized material properties and localized interphase stress distributions.* In order to validate the present theory in the micromechanical modeling of composites reinforced with coated particles,

$(R_c - R_p)/R_p$	CSA (GPa)	CPFBVP (GPa)	errors	MFBVP (GPa)	errors
Homogeneous	72.55	72.55	0.00%	72.55	0.00%
0	79.77	80.39	0.78%	79.81	0.05%
0.1	82.12	82.69	0.69%	82.17	0.06%
0.3	88.70	89.40	0.79%	88.89	0.21%
0.5	98.90	99.11	0.21%	99.27	0.37%

Table 4. Homogenized bulk modulus generated by the TCG and CSA models for various thicknesses of the coating.

both the homogenized bulk moduli as well as the local interphase stress distributions generated by the TCGs are compared with the composite sphere assemblage (CSA) model. The detailed derivation of CSA model is illustrated in the Appendix.

A TCG with the dimension of $L \times W \times H = 200 \times 200 \times 200 \, \mu m^3$ is used in this case and the particulate volume fraction is 10%. The material properties of the three constituents are listed in Table 1. For a better test of the TCG, the thickness of the coating is varied for comparison. Both MFBVP and CPFBVP are adopted to generate the bulk modulus. Table 4 shows that both methods generate well-matched predictions relative to the CSA model with the maximum error of less than 1%, and MFBVP usually generates smaller errors than CPFBVP for various thicknesses.

Then the local inter-phase stress concentrations are verified against CSA model. The stress components $\sigma_{xx}(z = 0)$, $\sigma_{yy}(z = 0)$, $\sigma_{xy}(z = 0)$ at the inner radius of coating (R_p) and the inner radius of the matrix (R_c) are thoroughly compared in Figures 5 and 6. Both MFBVP and CPFBVP agree well with the CSA results at the interface between the coating and matrix, while CPFBVP generates slightly offset results at the interface between the particle and coating relative to the other two methods.

Finally, the homogenized moduli are generated for a TCG with hard core/soft shell system, which has extensive applications in various structures [Xu et al. 2014a; 2014b]. In the present situation, the Young's modulus and bulk modulus generated by CPFBVP are compared with a very fine-mesh FEM [Tsui et al. 2001] and the CSA model, respectively. Figure 7 compares the generated homogenized moduli with material properties listed in Table 5. Three sets of thickness parameters are used for the comparison. Since the glass bead and Polycarbonate matrix are connected by a weak interphase, the overall moduli are decreased as the thickness of coating increases. It can be easily observed that the overall moduli computed by the TCGs are in good agreement with both the very detailed FE and the CSA results.

It should be pointed out that the CSA model usually generates reasonably accurate bulk modulus and only the upper and lower bounds of the Young's modulus for coated particulate composites. In addition, the phase-to-phase interaction is ignored within the model's assumptions, leading to inaccurate interphase stress fields for composites with large particulate volume fractions. Those concerns are alleviated in the TCGs, which adopt complete Trefftz solutions to calculate the effective properties and also recover exactly the local field concentrations at the interfaces of inhomogeneities. What's more, the effect of the locations of the particulates is also considered in the present technique, which cannot be easily captured by most of the existing methods.
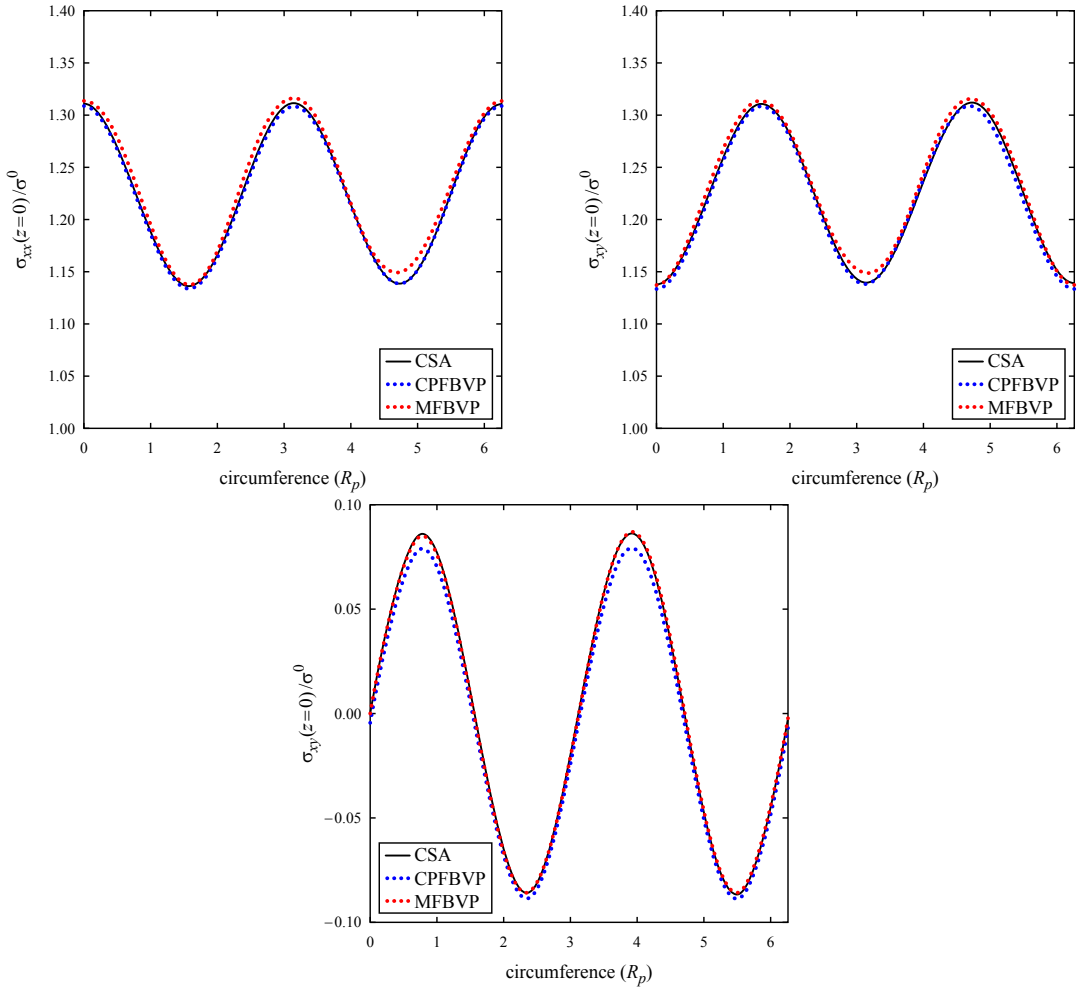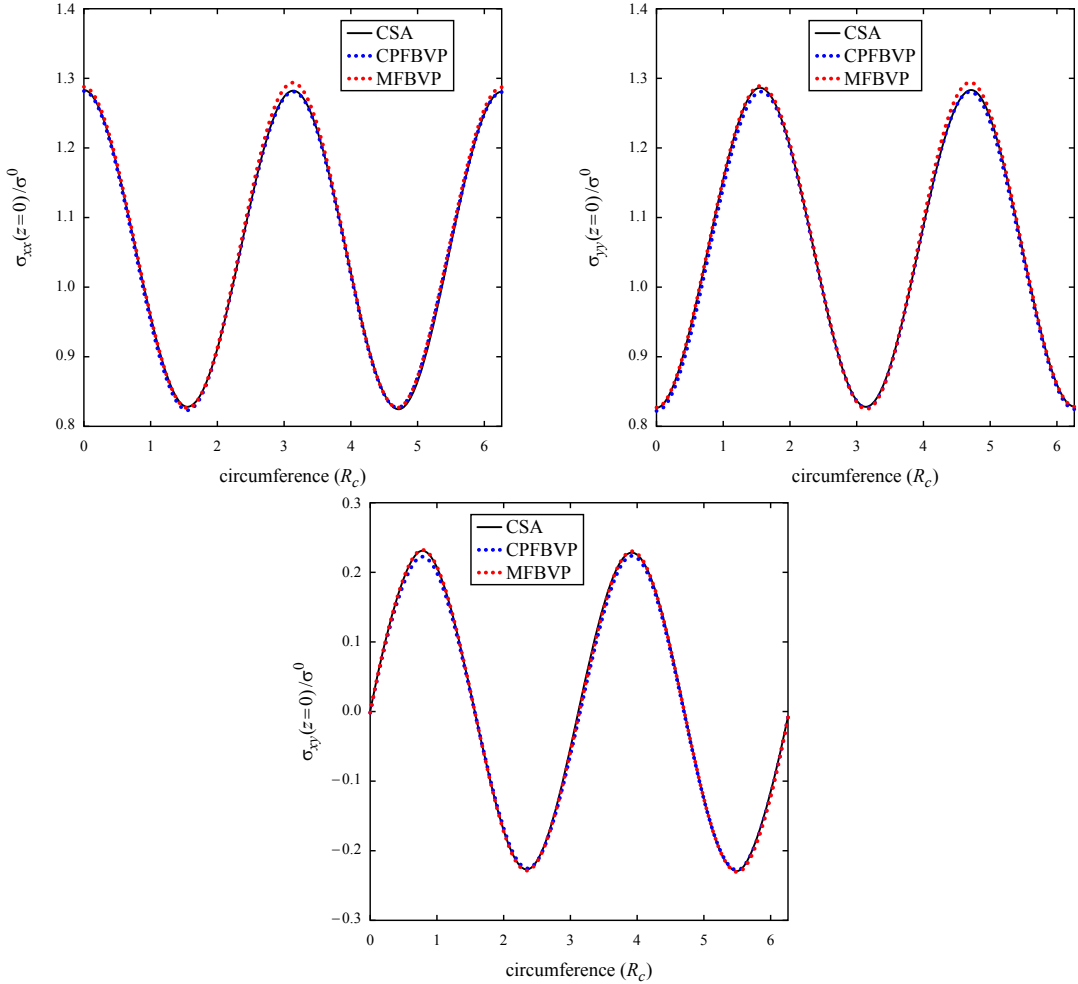
Figure 5. Variations of the three components $\sigma_{xx}(z=0)$, $\sigma_{yy}(z=0)$, $\sigma_{xy}(z=0)$ at the inner radius of the coating R_p.

	E (GPa)	ν
$4\,\mu$m Glass bead	70.0	0.22
Coating	0.50	0.30
Polycarbonate Matrix	2.28	0.38

Table 5. The material properties of a TCG with hard core/soft shell system.

4. Numerical studies

In the last section, the accuracy of the TCG is validated by generating the effective properties as well as the localized interphase stresses in composites with coated particles. In this section, we employ the TCGs

Figure 6. Variations of the three components $\sigma_{xx}(z=0)$, $\sigma_{yy}(z=0)$, $\sigma_{xy}(z=0)$ at the inner radius of matrix R_c.

to study the effect of coatings/interphases on the micromechanical behavior of composite materials. The Al$_2$O$_3$/Al particle/matrix system is adopted in this section, while the material properties and thickness of coating/interphase are varied.

4.1. *Effective properties.* In this example, A TCG is still employed with the dimensions of $L \times W \times H = 200 \times 200 \times 200\,\mu\mathrm{m}^3$ and the particle volume fraction of 0.2. The Young's modulus of the coating varies from 0 to 1000 GPa, and the ratio of thickness of the coating to the radius of the particle varies from 0 to 0.1. The homogenized moduli of the composite materials are illustrated in Figure 8. It can be easily observed that the homogenized moduli increase with the increase of the coating's moduli and thickness ($E_c/E_m \geq 1$). In addition, for a smaller magnitude of coating's material properties, the homogenized moduli of composites are very small no matter which thickness is adopted. This is due to the fact that
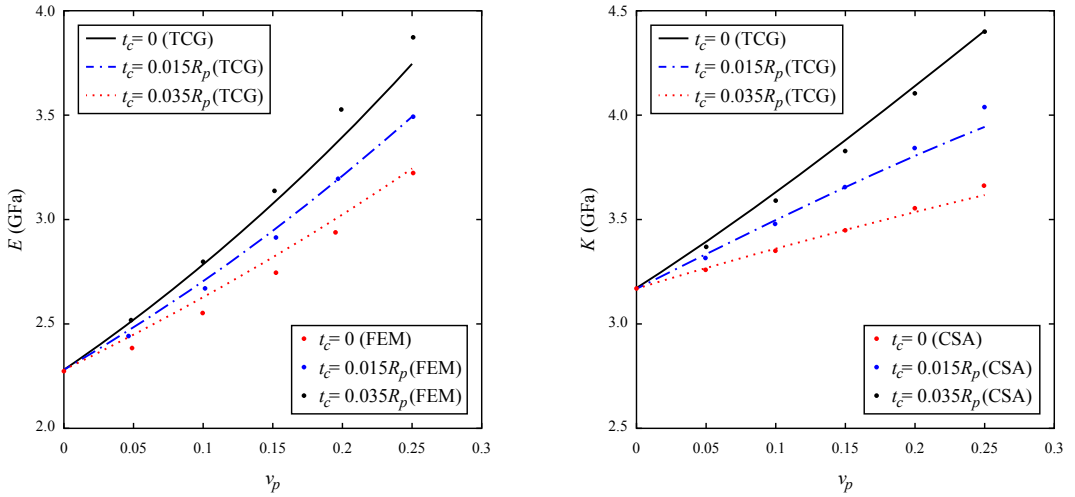
Figure 7. Comparison of (left) Young's moduli E and (right) bulk moduli K computed by using the TCGs, against the very fine-mesh FE and CSA results, respectively, for glass bead/polycarbonate composite with coatings of different thicknesses.
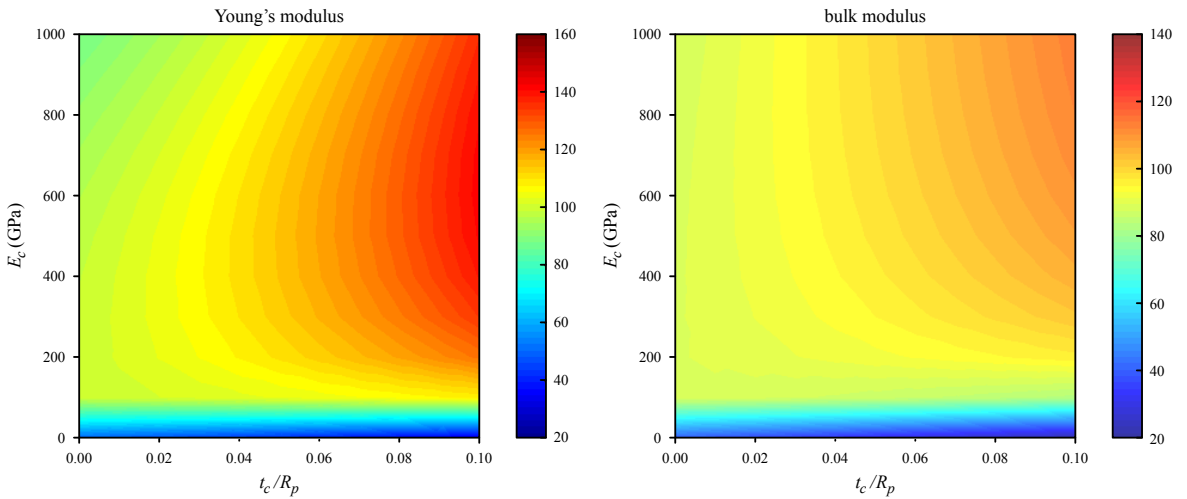
Figure 8. The effects of Young's modulus and thickness of the coating on the effective (left) Young's modulus and (right) bulk modulus of the composite.

the connection between fiber/matrix is very weak and the particle/coating domains can be treated as porosities.

4.2. *Local interphase stress concentrations.* The coating system plays an important role in the stress transfer between the constituents [Wang and Pindera 2016a]. Thus, herein the stress concentrations are studied by still tailoring the properties of the coatings. The definition of the stress concentration factor is $\text{SCF} = \sigma_{\theta\theta}/\sigma_{yy}^0$ in this situation. According to the transformations between the spherical and Cartesian
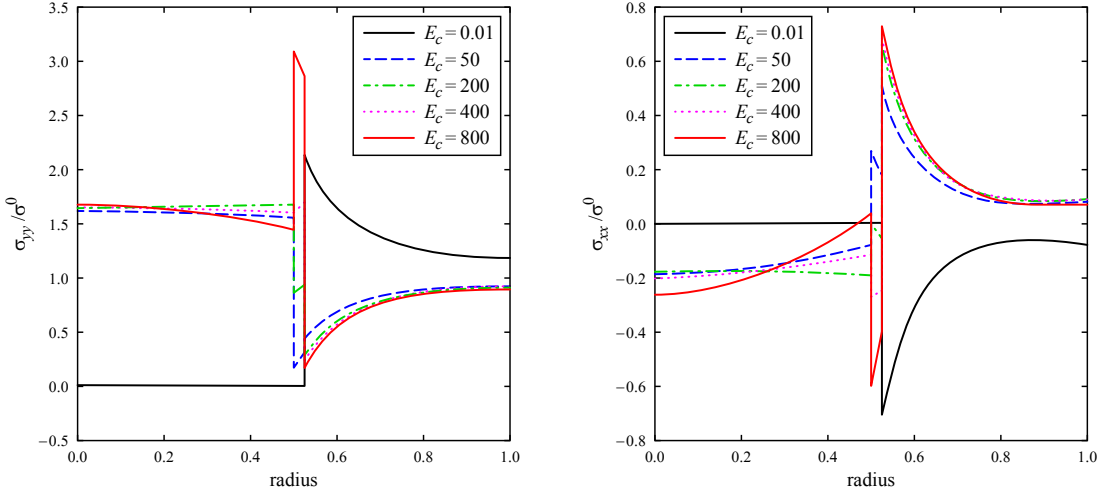
Figure 9. The effect of Young's modulus of the coating on the stress components $\sigma_{yy}(\theta = 0, \varphi = 0)$ and $\sigma_{xx}(\theta = \pi/2, \varphi = 0)$.

coordinates, $\sigma_{\theta\theta} = \sigma_{yy}(\theta = 0, \varphi = 0)$ and $\sigma_{\theta\theta} = \sigma_{xx}(\theta = \pi/2, \varphi = 0)$, SCF $= \sigma_{yy}/\sigma_{yy}^0$ at $\theta = 0$, $\varphi = 0$ locations and SCF $= \sigma_{xx}/\sigma_{yy}^0$ at $\theta = \pi/2$, $\varphi = 0$ locations.

The effect of the Young's modulus of the coating is firstly generated in Figure 9 by fixing its thickness as $t_c/R_p = 0.05$. The radius of the spherical particle is of one-quarter length of the TCG. The Young's modulus of the coating is varied from 0.01 GPa to 800 GPa. It can be easily observed that the largest SCFs occur at the interface between the coating and matrix. As is already mentioned before, when the coating has a low elastic modulus (0.01 GPa), the particle and coating can be treated as a porosity domain, and the corresponding stresses are essentially zeros (solid black line). When the modulus increases from 50 GPa to 800 GPa, the stress σ_{yy} at zero degree within the particle domain maintains within a narrow range of variations. Meanwhile, $\sigma_{yy}/\sigma_{yy}^0$ increases dramatically (from about 0.17 to over 3.09) in the coating domain, and then reduces and stabilizes at around 0.18 in the matrix phase. Conversely, the other component $\sigma_{xx}/\sigma_{yy}^0$ increases and stabilizes when E_c is larger than a certain amount, and shows more variations in the particle domain.

In contrast to the Young's modulus of the coating, the thickness of the coating plays a less important role in affecting the stress distributions, as illustrated in Figure 10. The magnitudes of the stresses barely change for different thicknesses. It should be noted that the SiC properties are used for the coating (Table 4) in this situation.

5. Implementation of periodic boundary conditions

To apply the periodic boundary conditions, the classical methods [Miehe and Koch 2002; Wang and Pindera 2016b] usually enforce the same values for the degrees of freedom of matching nodes on two opposite RVE sides. Thus, it requires a periodic mesh, which has the same mesh distribution on two opposite parts of the RVE boundary. However, the mesh of a TCG is generally nonperiodic so that the classical
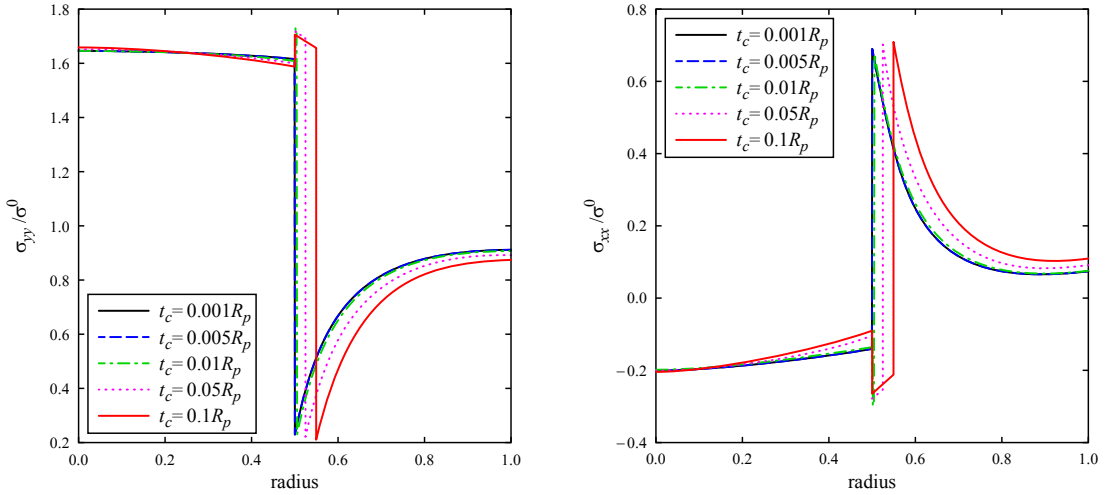
Figure 10. The effect of thickness of the coating on the stress components $\sigma_{yy}(\theta = 0, \varphi = 0)$ and $\sigma_{xx}(\theta = \pi/2, \varphi = 0)$.
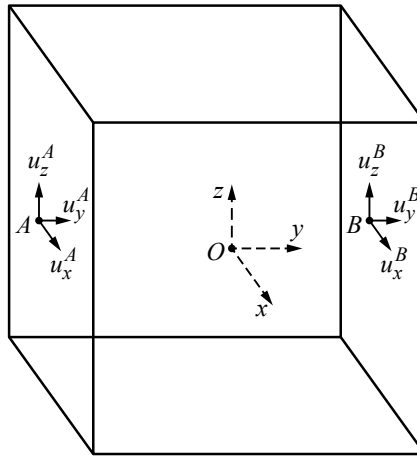

Figure 11. An RVE enforced with periodic displacement boundary conditions.

method cannot be directly employed. In this study, we developed a simple methodology to enforce periodic displacement boundary conditions on one RVE based on the surface-to-surface constraint scheme.

Figure 11 is a simple RVE with the origin point "O" located at the center. The point "A" is the mirror image of the point "B" relative to the original point. According to the reflectional symmetries with the reference to the $y = 0$ plane, the displacement components between "A" and "B" points should have the following relations [Drago and Pindera 2007]:

$$u_x^B - u_x^A = \bar{\varepsilon}_{xi} \cdot L_i, \quad u_y^B - u_y^A = \bar{\varepsilon}_{yi} \cdot L_i, \quad u_z^B - u_z^A = \bar{\varepsilon}_{zi} \cdot L_i, \tag{56}$$

where $i = x, y, z$. $\bar{\varepsilon}_{ij}$ is the macroscopic strain component and L_i is the dimension of the microstructure. Similar relations are applied to each pair of the symmetric points at the boundaries of the RVE.
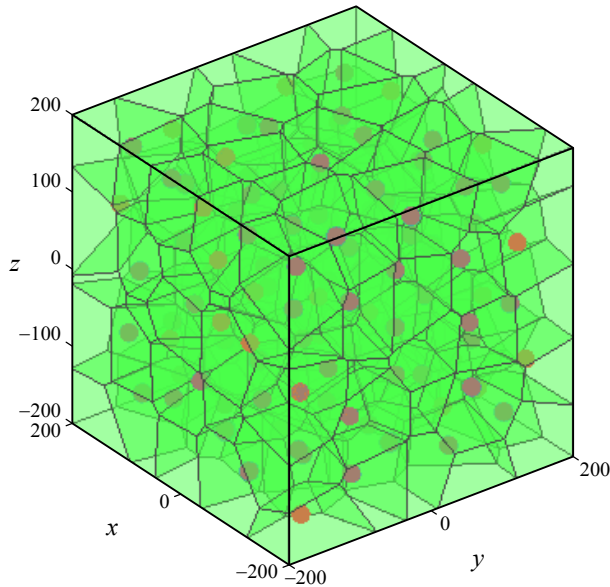
Figure 12. An RVE of 125 TCGs with the particle volume fraction of 1%.

Next an RVE including 125 coated spherical particles is considered in Figure 12, each particle is embedded within one TCG. The coating thickness is only 1% of the radius of the particle.

In a 3D RVE, the boundary points are composed of points on the six different faces, which are denoted as p_i^+ or p_i^- ($i = x, y, z$), where "+" and "−" signs stand for the positive and negative sides of the domain. Thus, the periodic boundary conditions are expressed as:

$$
\begin{aligned}
\boldsymbol{u}(p_x^+) - \boldsymbol{N}(p_x^-)\,\boldsymbol{u}(p_x^-) &= \bar{\boldsymbol{\varepsilon}} \cdot L_x, \\
\boldsymbol{u}(p_y^+) - \boldsymbol{N}(p_y^-)\,\boldsymbol{u}(p_y^-) &= \bar{\boldsymbol{\varepsilon}} \cdot L_y, \\
\boldsymbol{u}(p_z^+) - \boldsymbol{N}(p_z^-)\,\boldsymbol{u}(p_z^-) &= \bar{\boldsymbol{\varepsilon}} \cdot L_z,
\end{aligned}
\tag{57}
$$

where $\boldsymbol{u}$ is the displacement vector and $\bar{\boldsymbol{\varepsilon}}$ is the applied macroscopic strain. L_x, L_y, L_z are the dimensions of the RVE in the Cartesian coordinate. N is the interpolation function. After assembling the local stiffness matrices and equivalent nodal forces, the periodic boundary conditions can be directly enforced to the final global equations as essential boundary conditions, where all the nodal points at the boundaries of the RVE are involved. Equation (57) is applied at every boundary point on each face of RVE against its counterpart on the opposite face. For two points of the opposite faces which are exactly well matched, the periodic boundary conditions are easy to be applied by setting $N = 1$; while a point on one face which doesn't have the matched point on the other face, we locate the matched location, search the points close to this location, and apply the periodic conditions at those points using interpolations within the Wachspress coordinates [Dong and Atluri 2012b]. By validating the boundary conditions, we calculate the effective moduli by applying 1% macroscopic strain in the y-direction. Table 6 lists the generated results by assigning homogenous matrix properties (listed in Table 1) to the composite constituents, where the results perfectly recover the material properties of the matrix in the former case. In addition,

Material properties	E (GPa)	v
Homogeneous (matrix)	73.926	0.330
Composites	75.090	0.329

Table 6. Calculated effective properties by the RVE with 125 TCGs with different constituent properties.
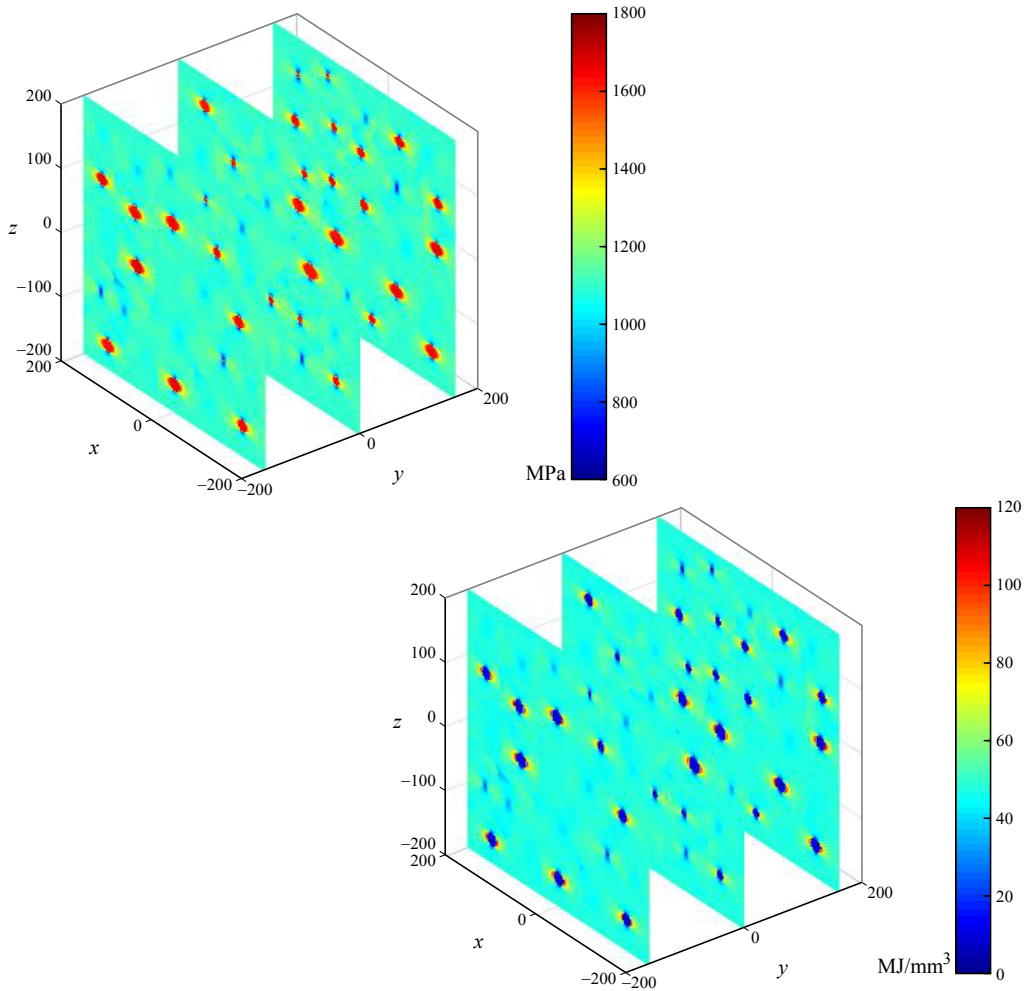

Figure 13. Distributions of (top) maximum principal stress (Unit: MPa) and (bottom) strain energy density (Unit: MJ/mm^3) in the RVE containing 125 coated particles.

the local field distributions are illustrated in Figure 13, where three cross-sections of the domain are focused upon. The principal stresses and energy densities are presented, and the concentrations always appear at the interfaces of the constituents, which help to identify the possible failure modes in the three-phase composite materials.

6. Conclusions

A Trefftz computational grain is developed based on the Voronoi Cell framework for the direct microme-chanical modeling of heterogeneous materials reinforced with coated particulate inclusions. In order to dramatically reduce the mesh discretization effort as well as the computational effort, each TCG is treated as a three-phase particle/coating/matrix grain, wherein the exact internal displacement field is assumed in terms of the P–N solutions that are further represented by the spherical harmonics. Two approaches are adopted to set up the local stiffness matrix of TCGs, where the MFBVP implements the continuity and boundary conditions through Lagrange multipliers, while the CPFBVP uses the collocation technique for continuity conditions and a primal variational principle for the boundary condition implementation. Both approaches generate accurate homogenized moduli as well as exact local interphase stress distributions, with good agreement to the very fine-mesh FE technique and the CSA model. The effects of the material properties as well as the thickness of the coating system on the effective properties and localized stress concentrations are also examined for the TCGs, where the former parameters play more important roles than the latter one in altering the response of composite materials. Finally, an easy implementation of periodic boundary conditions is applied on the RVEs through the surface-to-surface constraints of dis-placement field on the opposite faces. The developed TCGs provide accurate and efficient computational tools in the direct modeling of the micromechanical behavior of the particulate composites reinforced with coatings/interphases, which cannot be easily competed by the off-the-shelf FE packages and classical models.

Appendix: Derivation of CSA model.   The only existing Navier's equation for all the three phases is

$$\frac{d^2 u_r^{(k)}}{dr^2} + \frac{2}{r}\frac{d u_r^{(k)}}{dr} - \frac{2u_r^{(k)}}{r^2} = 0 \quad (k = p, c, m), \tag{A1}$$

which yields the displacement expression:

$$u_r^{(k)} = A^{(k)} r + B^{(k)}/r^2, \quad u_\theta^{(k)} = u_\varphi^{(k)} = 0. \tag{A2}$$

Through the strain-displacement and stress-strain relations, the stress components can be expressed as

$$\begin{aligned}
\sigma_{rr}^{(k)} &= 3K^{(k)} A^{(k)} - 4G^{(k)} B^{(k)}/r^3, \\
\sigma_{\theta\theta}^{(k)} &= 3K^{(k)} A^{(k)} + 2G^{(k)} B^{(k)}/r^3, \\
\sigma_{\varphi\varphi}^{(k)} &= 3K^{(k)} A^{(k)} + 2G^{(k)} B^{(k)}/r^3,
\end{aligned} \tag{A3}$$

where K and G are bulk and shear modulus of each phase. It should be noted that $B^{(p)} = 0$ since the displacements or stresses should be bounded at the origin of the particle phase. Beyond what is discussed above, the continuity conditions between the adjacent constituents are applied:

$$\begin{aligned}
u_r^{(p)}(r = a) &= u_r^{(c)}(r = a) \Rightarrow A^{(p)} a = A^{(c)} a + B^{(c)}/a^2, \\
\sigma_{rr}^{(p)}(r = a) &= \sigma_{rr}^{(c)}(r = a) \Rightarrow 3K^{(p)} A^{(p)} = 3K^{(c)} A^{(c)} - 4G^{(c)} B^{(c)}/a^3,
\end{aligned} \tag{A4}$$

$$\begin{aligned}
u_r^{(c)}(r = b) &= u_r^{(m)}(r = b) \Rightarrow A^{(c)} b + B^{(c)}/b^2 = A^{(m)} b + B^{(m)}/b^2, \\
\sigma_{rr}^{(c)}(r = b) &= \sigma_{rr}^{(m)}(r = b) \Rightarrow 3K^{(c)} A^{(c)} - 4G^{(c)} B^{(c)}/b^3 = 3K^{(m)} A^{(m)} - 4G^{(m)} B^{(m)}/b^3.
\end{aligned} \tag{A5}$$

In addition, a homogeneous surface stress loading σ^0 is applied at the outermost radius ($r = c$) to calculate the bulk modulus, and

$$\sigma_{rr}^{(m)}(r = c) = \sigma^0 \Rightarrow 3K^{(m)}A^{(m)} - 4G^{(m)}B^{(m)}/c^3 = \sigma^0. \tag{A6}$$

Thus, five equations are established for the five unknowns $A^{(p)}$, $A^{(c)}$, $B^{(c)}$, $A^{(m)}$, $B^{(m)}$, and finally, through the definition of bulk modulus:

$$K^* = \frac{\sigma_{rr}^{(m)}(r = c)}{u_r^{(m)}(r = c)/c}. \tag{A7}$$

The replacement scheme is also used by Qiu and Weng [1991] to obtain the exact expression of the homogenized bulk modulus for the three-phase composites, which is also programmed to validate the above equations.

Acknowledgement

References

[Babuška 1973] I. Babuška, "The finite element method with Lagrange multipliers", *Numer. Math.* **20**:3 (1973), 179–192.

[Bishay and Atluri 2013] P. L. Bishay and S. N. Atluri, "2D and 3D multiphysics Voronoi cells based on radial basis functions, for Direct Mesoscale Numerical Simulation (DMNS) of the switching phenomena in ferroelectric polycrystalline materials", *CMC: Comput. Mater. Con.* **33**:1 (2013), 19–62.

[Bishay and Atluri 2014] P. L. Bishay and S. N. Atluri, "Trefftz-Lekhnitskii Grains (TLGs) for Efficient Direct Numerical Simulation (DNS) of the micro/meso mechanics of porous piezoelectric materials", *Comput. Mater. Sci.* **83** (2014), 235–249.

[Bishay and Atluri 2015] P. L. Bishay and S. N. Atluri, "Computational Piezo-Grains (CPGs) for a highly-efficient microme-chanical modeling of heterogeneous piezoelectric-piezomagnetic composites", *Eur. J. Mech. A Solids* **53** (2015), 311–328.

[Bishay et al. 2014] P. L. Bishay, A. Alotaibi, and S. N. Atluri, "Multi-Region Trefftz Collocation Grains (MTCGs) for model-ing piezoelectric composites and porous materials in direct and inverse problems", *J. Mech. Mater. Struct.* **9**:3 (2014), 287–312.

[Brezzi 1974] F. Brezzi, "On the existence, uniqueness and approximation of saddle-point problems arising from Lagrange multipliers", *ESAIM: Math. Model. Numer. Anal.* **8** (1974), 129–151.

[Chen et al. 2016] Q. Chen, X. Chen, Z. Zhai, and Z. Yang, "A new and general formulation of three-dimensional finite-volume micromechanics for particulate reinforced composites with viscoplastic phases", *Compos. B Eng.* **85** (2016), 216–232.

[Chen et al. 2017] Q. Chen, G. Wang, X. Chen, and J. Geng, "Finite-volume homogenization of elastic/viscoelastic periodic materials", *Compos. Struct.* **182** (2017), 457–470.

[Cherkaoui et al. 1994] M. Cherkaoui, H. Sabar, and M. Berveiller, "Micromechanics approach of the coated inclusion problem and applications to composite materials", *J. Eng. Mater. Technol.* (*ASME*) **116**:3 (1994), 274–278.

[Dong and Atluri 2012a] L. Dong and S. N. Atluri, "Trefftz Voronoi cells with elastic/rigid inclusions or voids for microme-chanical analysis of composite and porous materials", *Comput. Model. Eng. Sci.* **83**:2 (2012), 183–220.

[Dong and Atluri 2012b] L. Dong and S. N. Atluri, "Development of 3D Trefftz Voronoi cells with/without spherical voids &/or elastic/rigid inclusions for micromechanical modeling of heterogeneous materials", *CMC: Comput. Mater. Con.* **29**:2 (2012), 169–212.

[Dong and Atluri 2012c] L. Dong and S. N. Atluri, "Development of 3D Trefftz Voronoi cells with ellipsoidal voids &/or elastic/rigid inclusions for micromechanical modeling of heterogeneous materials", *CMC: Comput. Mater. Con.* **30**:1 (2012), 31–81.

[Drago and Pindera 2007] A. Drago and M.-J. Pindera, "Micro-macromechanical analysis of heterogeneous materials: Macro-scopically homogeneous vs periodic microstructures", *Compos. Sci. Technol.* **67**:6 (2007), 1243–1263.

[Ghosh et al. 1995] S. Ghosh, K. Lee, and S. Moorthy, "Multiple scale analysis of heterogeneous elastic structures using homogenization theory and voronoi cell finite element method", *Int. J. Solids Struct.* **32**:1 (1995), 27–62.

[Hashin 1962] Z. Hashin, "The elastic moduli of heterogeneous materials", *J. Appl. Mech.* (*ASME*) **29** (1962), 143–150.

[Herve and Zaoui 1993] E. Herve and A. Zaoui, "*n*-Layered inclusion-based micromechanical modelling", *Int. J. Eng. Sci.* **31**:1 (1993), 1–10.

[Jiang et al. 2008] Y. Jiang, W. Guo, and H. Yang, "Numerical studies on the effective shear modulus of particle reinforced composites with an inhomogeneous inter-phase", *Comput. Mater. Sci.* **43**:4 (2008), 724–731.

[Jiang et al. 2009] Y. Jiang, K. Tohgo, and Y. Shimamura, "A micro-mechanics model for composites reinforced by regularly distributed particles with an inhomogeneous interphase", *Comput. Mater. Sci.* **46**:2 (2009), 507–515.

[Liu 2007a] C.-S. Liu, "A modified Trefftz method for two-dimensional Laplace equations considering the domain's characteristic length", *Comput. Model. Eng. Sci.* **21**:1 (2007), 53–65.

[Liu 2007b] C.-S. Liu, "An effectively modified direct Trefftz method for 2D potential problems considering the domain's characteristic length", *Eng. Anal. Bound. Elem.* **31**:12 (2007), 983–993.

[Liu et al. 2005] D. S. Liu, C. Y. Chen, and D. Y. Chiou, "3-D Modeling of a composite material reinforced with multiple thickly coated particles using the infinite element method", *Comput. Model. Eng. Sci.* **9**:2 (2005), 179–191.

[Lurie 2005] A. I. Lurie, *Theory of elasticity*, 4th ed., Springer, 2005.

[Marur 2004] P. R. Marur, "Estimation of effective elastic properties and interface stress concentrations in particulate composites by unit cell methods", *Acta Mater.* **52**:5 (2004), 1263–1270.

[Michel et al. 2000] J. C. Michel, H. Moulinec, and P. Suquet, "A computational method based on augmented Lagrangians and fast Fourier transforms for composites with high contrast", *Comput. Model. Eng. Sci.* **1**:2 (2000), 79–88.

[Miehe and Koch 2002] C. Miehe and A. Koch, "Computational micro-to-macro transitions of discretized microstructures undergoing small strains", *Arch. Appl. Mech.* **72**:4-5 (2002), 300–317.

[Moorthy and Ghosh 1998] S. Moorthy and S. Ghosh, "A Voronoi Cell finite element model for particle cracking in elastic-plastic composite materials", *Comput. Methods Appl. Mech. Eng.* **151**:3 (1998), 377–400.

[Moulinec and Suquet 1998] H. Moulinec and P. Suquet, "A numerical method for computing the overall response of nonlinear composites with complex microstructure", *Comput. Methods Appl. Mech. Eng.* **157**:1 (1998), 69–94.

[Neuber 1934] H. Neuber, "Ein neuer Ansatz zur Lösung räumlicher Probleme der Elastizitätstheorie", *J. Appl. Math. Mech.* **14**:4 (1934), 203–212.

[Nguyen et al. 2011] N. B. Nguyen, A. Giraud, and D. Grgic, "A composite sphere assemblage model for porous oolitic rocks", *Int. J. Rock Mech. Min.* **48**:6 (2011), 909–921.

[Papkovish 1932] P. F. Papkovish, "Solution Générale des équations differentielles fondamentales d'élasticité exprimée par trois fonctions harmoniques", *C. R. Math. Acad. Sci. Paris* **195** (1932), 513–515.

[Punch and Atluri 1984] E. F. Punch and S. N. Atluri, "Development and testing of stable, invariant, isoparametric curvilinear 2- and 3-D hybrid-stress elements", *Comput. Methods Appl. Mech. Eng.* **47**:3 (1984), 331–356.

[Qin 2005] Q.-H. Qin, "Trefftz finite element method and its applications", *Appl. Mech. Rev.* (*ASME*) **58** (2005), 316–337.

[Qiu and Weng 1991] Y. P. Qiu and G. J. Weng, "Elastic moduli of thickly coated particle and fiber-reinforced composites", *J. Appl. Mech.* (*ASME*) **58** (1991), 388–398.

[Quang and He 2007] H. L. Quang and Q.-C. He, "A one-parameter generalized self-consistent model for isotropic multiphase composites", *Int. J. Solids Struct.* **44**:21 (2007), 6805–6825.

[Rubinstein et al. 1983] R. Rubinstein, E. F. Punch, and S. N. Atluri, "An analysis of, and remedies for, kinematic modes in hybrid-stress finite elements: selection of stable, invariant stress fields", *Comput. Methods Appl. Mech. Eng.* **38**:1 (1983), 63–92.

[Tsui et al. 2001] C. P. Tsui, C. Y. Tang, and T. C. Lee, "Finite element analysis of polymer composites filled by interphase coated particles", *J. Mater. Process. Technol.* **117**:1 (2001), 105–110.

[Tsui et al. 2006] C. P. Tsui, D. Z. Chen, C. Y. Tang, P. S. Uskokovic, J. P. Fan, and X. L. Xie, "Prediction for debonding damage process and effective elastic properties of glass-bead-filled modified polyphenylene oxide", *Compos. Sci. Technol.* **66**:11 (2006), 1521–1531.

[Wachspress 1975] E. Wachspress, *A rational finite element basis*, Academic Press, New York, 1975.

[Wang and Pindera 2016a] G. Wang and M.-J. Pindera, "Locally-exact homogenization of unidirectional composites with coated or hollow reinforcement", *Mater. Des.* **93** (2016), 514–528.

[Wang and Pindera 2016b] G. Wang and M.-J. Pindera, "On boundary condition implementation via variational principle in elasticity-based homogenization", *J. Appl. Mech.* (*ASME*) **83**:10 (2016), 101008.

[Wang et al. 2018] G. Wang, L. Dong, and S. N. Atluri, "A Trefftz collocation method (TCM) for three-dimensional linear elasticity by using the Papkovich-Neuber solutions with cylindrical harmonics", *Eng. Anal. Bound. Elem.* **88** (2018), 93–103.

[Xu et al. 2014a] W. Xu, H. Chen, W. Chen, and L. Jiang, "Prediction of transport behaviors of particulate composites considering microstructures of soft interfacial layers around ellipsoidal aggregate particles", *Soft Matter* **20** (2014), 627–638.

[Xu et al. 2014b] W. Xu, W. Chen, and H. Chen, "Modeling of soft interfacial volume fraction in composite materials with complex convex particles", *J. Chem. Phys.* **140** (2014), 034704.

[Yvonnet et al. 2011] J. Yvonnet, Q.-C. He, Q.-Z. Zhu, and J.-F. Shao, "A general and efficient computational procedure for modelling the Kapitza thermal resistance based on XFEM", *Comput. Mater. Sci.* **50**:4 (2011), 1220–1224.

[Zhang et al. 2007] W. X. Zhang, L. X. Li, and T. J. Wang, "Interphase effect on the strengthening behavior of particle-reinforced metal matrix composites", *Comput. Mater. Sci.* **41**:2 (2007), 145–155.

[Zhu et al. 2011] Q.-Z. Zhu, S.-T. Gu, J. Yvonnet, J.-F. Shao, and Q.-C. He, "Three-dimensional numerical modelling by XFEM of spring-layer imperfect curved interfaces with applications to linearly elastic composite materials", *Int. J. Numer. Methods Eng.* **88**:4 (2011), 307–328.

GUANNAN WANG: gw5qv@virginia.edu
Center for Advanced Research in the Engineering Sciences, Texas Tech University, Lubbock, TX, United States

and

Department of Mechanical Engineering, Texas Tech University, Lubbock, TX, United States

LEITING DONG: ltdong@buaa.edu.cn
School of Aeronautic Science and Engineering, Beihang University, Beijing, China

JUNBO WANG: junbowang@outlook.com
School of Aeronautic Science and Engineering, Beihang University, Beijing, China

SATYA N. ATLURI: snatluri.ttu@gmail.com
Center for Advanced Research in the Engineering Sciences, Texas Tech University, Lubbock, TX, United States

and

Department of Mechanical Engineering, Texas Tech University, Lubbock, TX, United States

JOURNAL OF MECHANICS OF MATERIALS AND STRUCTURES

msp.org/jomms

Founded by Charles R. Steele and Marie-Louise Steele

Journal of Mechanics of Materials and Structures